Dalton Transactions

ROYAL SOCIETY OF CHEMISTRY

PAPER

View Article Online
View Journal | View Issue

Cite this: *Dalton Trans.*, 2025, **54**, 15290

Simultaneous electrochemical sensing of Pb^{2+} and Hg^{2+} in aqueous media using 5-amino-1,3,4-thiadiazole-2-thiol functionalized mesoporous silica

Bipasha Saha,[a,b] Manjula Pal,[a] Hiroshi Uyama [c] and Mahasweta Nandi *[a]

Metal ion pollution is a major environmental concern, with toxic metals like lead (Pb) and mercury (Hg) contaminating water, soil and air, which poses serious risks to human health and the ecosystem. Thus, effective monitoring is essential to assess and mitigate their harmful impact. Electrochemical metal ion sensing has emerged as a promising real-time technique for quantifying metal ions through electrode reactions with high accuracy, sensitivity and selectivity. For this purpose, a thiol-functionalized silica supported material, **FMS-TA-ATT**, has been synthesized for the electrochemical sensing of Pb^{2+} and Hg^{2+} simultaneously and individually in 0.2 M acetate buffer solution and is found to hold promising detection ability in neutral medium (pH = 7). The comprehensive characterization of the synthesized materials has been performed by powder X-ray diffraction, electron microscopy, nitrogen adsorption/desorption studies, thermogravimetric analysis, FT-IR, and solid state ^{29}Si and ^{13}C CP MAS NMR spectroscopy, and the electrochemical behavior has been evaluated by cyclic voltammetry and electrochemical impedance spectroscopy. The sensing ability of the glassy carbon electrode prepared with **FMS-TA-ATT** (**FMS-TA-ATT/GCE**) has been examined by differential pulse voltammetry. This material shows good selectivity and sensitivity towards Pb^{2+} and Hg^{2+} in 0.2 M acetate buffer solution at pH = 7 with a very low limit of detection (LOD) (13 nM for Pb^{2+} and 29 nM for Hg^{2+}). Additionally, **FMS-TA-ATT/GCE** is efficient at detecting Pb^{2+} and Hg^{2+} in the presence of other metal ions and it also displays sensing ability with real water samples.

Received 9th July 2025,
Accepted 6th September 2025

DOI: 10.1039/d5dt01618e

rsc.li/dalton

Introduction

The detection of heavy metal ions (typically having atomic densities above 4.0 to 4.5 g cm^{-3}) and the determination of their quantities in various water reserves and the environment are of immense importance because their presence above the threshold values poses several invisible threats to human health and other living organisms. Several international organizations like the World Health Organization (WHO), the Joint Food and Agricultural Organization (FAO), the US Environmental Protection Agency (EPA), the Centre for Disease Control (CDC) and the European Union provide guidance and recommend limits for water quality, which serves as a basis for developing the national standards. The heavy metal ions like lead and mercury can easily get accumulated in the living organisms through various biological chains by reactions with sulphur containing proteins and enzymes[1] and lead to neurological and nephrological disorders.[2,3] Pb^{2+} has a tendency to get accumulated in teeth and bones, which causes irreversible damage to nervous and digestive systems,[4] whereas Hg^{2+} strongly interferes with nervous and endocrine systems.[5] Identification of heavy metal ions requires the development of highly sensitive and selective techniques that can detect trace levels of ions in various complex matrices like biological samples (blood, serum, saliva, *etc.*), natural and waste water, food, air and soil. There are several spectroscopic techniques that have been developed to monitor the presence of heavy metal ions,[6] such as atomic absorption spectroscopy,[7] X-ray fluorescence spectroscopy,[8] inductively coupled plasma-optical emission spectrometry (ICP-OES),[9] optical sensing,[10] *etc.* Although these techniques enable the detection of multiple metal ions with good detection sensitivity, the expensive equipment, high running cost, complex sample preparation and elaborate analytical procedures limit their applications considerably. To overcome these problems, electrochemical sensing can be a good alternative to detect these metal ions.

[a]*Integrated Science Education and Research Centre, Siksha Bhavana, Visva-Bharati University, Santiniketan 731 235, India.*
E-mail: mahasweta.nandi@visva-bharati.ac.in
[b]*Department of Chemistry, Siksha Bhavana, Visva-Bharati University, Santiniketan 731 235, India*
[c]*Department of Applied Chemistry, Graduate School of Engineering, Osaka University, 2-1 Yamadaoka, Suita, Osaka, 565-0871, Japan*

An electrochemical sensing technique detects and quantifies different analytes by measuring the changes in the electrical properties through amperometry, potentiometry and conductometry.[11] This process has numerous advantages in various applications like healthcare, environmental monitoring, industrial processes, *etc*. Electrochemical sensors are highly selective in nature as well as sensitive in detecting trace levels of analytes. The selectivity of such sensors can be tuned by varying different parameters and the methods are cost effective and less time consuming, making them useful in monitoring the process. Electrochemical sensors are not only used to sense metal ions[12] but can also be used to detect liquids,[13] gases[14] and even biomolecules.[15] Among the different types of electrochemical sensing procedures, voltammetry is most commonly used where current is measured as a function of applied potential like cyclic voltammetry, differential pulse voltammetry, square wave voltammetry, *etc*. Of these, differential pulse voltammetry (DPV) is of particular interest due to its superior sensitivity and hence it is employed extensively in the area of biosensing and chemical sensing. The higher sensitivity of DPV is attributed to the fact that the background current arising from the interfacial capacitance is marginally affected by the small changes in the applied potential. Thus, from the difference in the currents in two measurements carried out over a small potential difference, the effect of background current can be minimized offering higher sensitivity towards the faradaic current that arises from electron transfer in a chemical reaction.[16]

To carry out electrochemical sensing, a suitable electrode material is essential and, in this context, organic compound-based sensors[17,18] and functionalized mesoporous silica-based sensors can be considered as potential candidates.[19] Ordered mesoporous silicas are versatile solid supports by virtue of their properties such as a large surface area, tunable pore size, high pore volume, biocompatibility, *etc.* and have found extensive use in the fields of catalysis,[20] adsorption[21] and sensing.[22] In spite of their low electrical conductivity, they can be used in the preparation of electrodes because of their high adsorption capacity, which enables the electroactive analytes to get adsorbed on their surface prior to the electrochemical detection.[23] Being non-conductors themselves, the silica support does not contribute to the charging current when used in the modification of the electrodes, thereby giving a very low background.[24] On the other hand, mesoporous silica supports can be modified at their surface silanol sites with a host of organic functional groups through covalent interactions. Such functionalization prevents the leaching of the organic moieties from the electrode surface, giving stability to the electrodes and facilitating the electrode reaction.[25] For the sensing of heavy metal ions like lead and mercury, which are so called soft Lewis acids, it is desirable that the organic electroactive moiety projects soft binding centers towards the metal ions.[26] In this respect, sulphur donor sites are useful with a wide possibility of organic precursors available.[27] Recent literature studies have indicated that detection of heavy metal ions is accomplished mostly in acidic medium (*i.e.* pH < 7).[28,29] However, for practical utility and applications in biological systems, it is always desirable that the sensing mechanism operate in a neutral medium.

To address the above issues, in the present study we report a functionalized mesoporous silica-based material, **FMS-TA-ATT**, for the sensing of Pb^{2+} and Hg^{2+} using differential pulse voltammetry in aqueous medium and at neutral pH. **FMS-TA-ATT** has been synthesized by stepwise functionalization of an SBA-15 type mesoporous silica by 3-aminopropyl triethoxysilane (3-APTES), tris-(4-formyl phenyl) amine and 5-amino-1,3,4-thiadiazole-2-thiol, respectively (Scheme 1). The resulting material contains multiple nitrogen and sulphur donor sites which can individually and simultaneously sense Pb^{2+} and Hg^{2+} in aqueous medium with two distinct peak positions in 0.2 M acetate buffer solution adjusted to pH = 7. Selective sensing of these heavy metal ions in neutral aqueous medium is highly significant for identifying metal ion pollution in the environment. A survey of the sensing properties of **FMS-TA-ATT** with real water samples collected from various sources shows that the material is efficient at detecting Pb^{2+} and Hg^{2+} from the as-collected water in the absence of any electrolyte, including 0.2 M acetate buffer.

Experimental section

Materials and physical methods

Tetraethyl orthosilicate (TEOS), poly(ethylene glycol)-*block*-poly (propylene glycol)-*block*-poly(ethylene glycol) (Pluronic P123), 3-aminopropyl triethoxysilane (3-APTES), triphenyl amine, 5-amino-1,3,4-thiadiazole-2-thiol and chloroform-d ($CDCl_3$) were purchased from Sigma Aldrich and used without further purification. Phosphoryl chloride ($POCl_3$) was procured from Spectrochem India. Hydrochloric acid (HCl), nitric acid (HNO_3), sodium hydroxide (NaOH), sodium sulphate (Na_2SO_4), dimethyl formamide (DMF), chloroform, dichloromethane (DCM), sodium acetate (NaAc), acetic acid (HAc), different metal salts and other chemicals were purchased from E-Merck and used as received. The solvents used for spectroscopic studies were purified and dried following the standard literature procedure.[30]

The ^{1}H NMR spectrum was determined at 400 MHz using a Bruker NMR spectrometer as a solution in $CDCl_3$. Chemical shifts are expressed in parts per million (δ) and the signals are reported as s (singlet) and d (doublet). The $^{13}C\{^1H\}$ NMR spectrum was recorded at 100 MHz in $CDCl_3$. Chemical shifts as an internal standard are referenced to $CDCl_3$ (δ = 7.26 for ^{1}H and δ = 77.16 for $^{13}C\{^1H\}$ NMR). Powder X-ray diffraction (PXRD) of the samples was carried out in a Bruker D8 Advance instrument equipped with Ni-filtered Cu-Kα radiation (λ = 1.5406 Å) and operated at 40 kV and 40 mA. A field emission-scanning electron microscopy (FE-SEM) image has been captured using a Gemini SEM 450 (Zeiss) microscope coupled with an EDAX Ametek (Model: Element) energy dispersive spectroscopy (EDS) attachment. A transmission electron microscopy (TEM) image of the mesoporous silica support was captured in a UHR-FEG

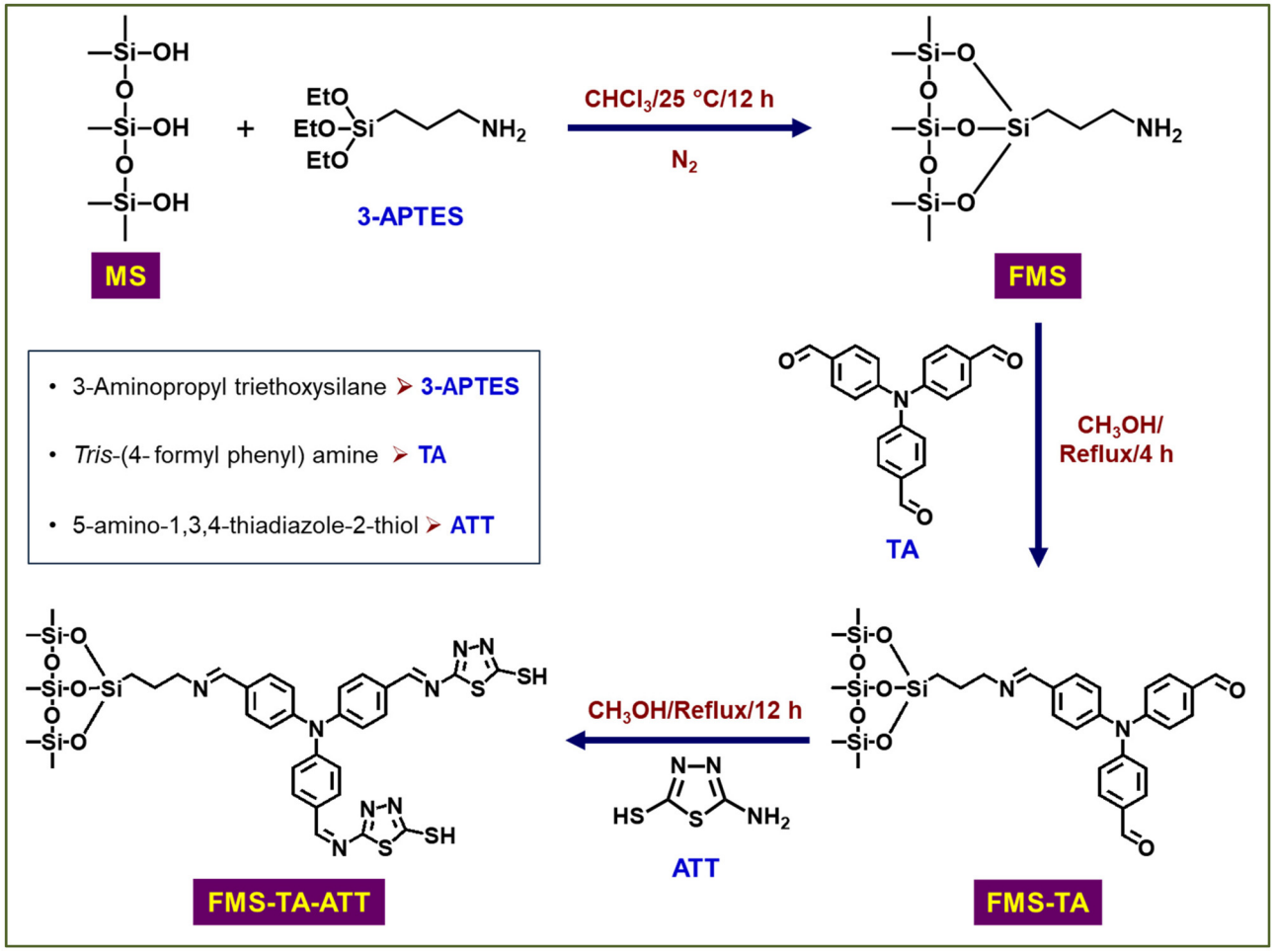

Scheme 1 Synthesis of **FMS-TA-ATT**.

(ultrahigh resolution-field emission electron gun) JEOL JEM 2100F transmission electron microscope operated at 200 kV. The sample grid was prepared by drop-casting the sample dispersed in 2-propanol on a copper grid (400 mesh) coated with amorphous carbon. Nitrogen adsorption/desorption isotherms at various stages of the syntheses were studied at 77 K using a NOVA 2200e (Quantachrome Instruments) surface area and pore size analyzer. The samples were degassed before the measurements at 333 K for 6 h for the organic–inorganic hybrid structures and 393 K for 4 h for the pure mesoporous silica. The multipoint BET (Brunauer–Emmett–Teller) method was used to determine the specific surface areas whereas the NLDFT (non-local density functional theory) model was used to obtain the pore size distributions. FT-IR spectra of the mesoporous silica and the subsequent functionalized samples were recorded on an IRAffinity-1S Fourier transform infrared spectrometer (Shimadzu) using KBr pellets. Prior to the measurements, all the samples were preheated overnight at 333 K to remove the physisorbed solvent molecules. Solid state ^{29}Si and ^{13}C CP MAS NMR analyses were carried out in a CHEMAGNETICS 300 MHz CMX 300 spectrometer. Thermogravimetric analyses (TGAs) of the samples were carried out under the flow of oxygen (100 mL min^{-1}) using a TA SDT 650 (Waters) instrument from 303 to 1073 K, at a heating rate of 10 K min^{-1}. All electrochemical studies, *e.g.* cyclic voltammetry (CV), differential pulse voltammetry (DPV) and electrochemical impedance spectroscopy (EIS), were carried out using a Metrohm AUTOLAB PGSTAT-128N instrument equipped with a three-electrode setup in 0.2 M acetate (sodium acetate, NaAc/acetic acid, HAc) buffer solution. The samples deposited over a 5 mm glassy carbon electrode (GCE) were used as the working electrode, a saturated calomel electrode (SCE) as the reference electrode and a platinum plate (2 cm × 1 cm) as the counter electrode.[31]

Synthesis

SBA-15 type mesoporous silica was synthesized following a literature method.[32] In a typical procedure, 1.7 g of Pluronic P123 was dissolved in 62 mL of distilled water under stirring in a polypropylene bottle. 6.0 g of 35% HCl was added to the resulting clear solution and after 30 min of stirring, 3.5 g of TEOS was added slowly to it. The mixture was kept under stirring at 313 K for 20 h when a white gel was formed. The bottle with the gel was capped tightly and transferred into an oven

where it was heated for another 24 h at 373 K without stirring. The product obtained was filtered, washed several times with water followed by ethanol and dried under vacuum. The resulting white powder was calcined at 773 K for 10 h to obtain SBA-15 type mesoporous silica (**MS**). In the next step, 1.0 g of **MS** was taken in 150 mL of chloroform and 1.5 g of 3-APTES was added to it. The mixture was stirred for 12 h at ambient temperature under a nitrogen atmosphere and the resulting solid was filtered, washed thoroughly with chloroform and then dichloromethane and dried to obtain the white product of 3-APTES functionalized mesoporous silica, **FMS**. This NH_2-grafted silica (0.25 g) was subsequently allowed to react with the –CHO group of tris-(4-formyl phenyl) amine (TA, 0.15 g) maintaining a mole ratio of 1 : 1, in 15 mL of methanol under refluxing conditions for 4 h (Scheme 1). Tris-(4-formyl phenyl) amine was prepared using a Vilsmeier–Haack formylation reaction of triphenyl amine[33] and the details of its synthesis and the NMR spectrum are given in the SI. At this stage, the reaction mixture becomes yellow and the trialdehyde functionalized solid product, **FMS-TA**, is separated out by filtration, washed with methanol and dried under vacuum. In the final step, 0.05 g of **FMS-TA** was allowed to react with 0.05 g of 5-amino-1,3,4-thiadiazole-2-thiol (excess) in 15 mL of methanol under reflux for 12 h. The yellow product (**FMS-TA-ATT**) after isolation by filtration, washing with methanol and drying under vacuum has been used as the probe in the electrochemical metal ion-sensing studies.

Electrochemical performance test

At first, the glassy carbon electrode (GCE) was polished on a felt pad with 0.05 mm aluminum, then ultrasonically treated in alcohol and rinsed with deionized water. Then, 10 mg of the sample (**MS** or **FMS** or **FMS-TA** or **FMS-TA-ATT**) was dispersed in 1 mL of ethanol and ultrasonically treated for 60 min to form a uniform dispersion. Finally, 10 μL of the dispersion was drop-cast on the GCE and dried under vacuum to fabricate the **MS**, **FMS**, **FMS-TA** and **FMS-TA-ATT**-deposited glassy carbon electrode, designated as **MS/GCE**, **FMS/GCE**, **FMS-TA/GCE** and **FMS-TA-ATT/GCE**, respectively. These electrodes were used for electrochemical studies. Electrochemical detection methods for metal ion sensing including cyclic voltammetry (CV), electrochemical impedance spectroscopy (EIS) and differential pulse voltammetry (DPV) were performed. The electrochemical performance of the prepared electrodes was determined by CV and EIS in 5 mM $[Fe(CN)_6]^{3-/4-}$ (1 : 1 molar ratio) solution containing 0.1 M KCl. The cyclic voltammograms of the samples were performed within the potential window of −1.0 to +1.1 V in a three-electrode set-up. The EIS characterization conditions were set from 10^5 Hz to 0.1 Hz. The detection of Pb^{2+} and Hg^{2+} by DPV was carried out in a 0.2 M acetate buffer solution adjusted to pH = 7 using 1 M NaOH solution with an operating voltage range from −0.9 to +0.8 V, where the amplitude is 0.025 V, the deposition voltage is −0.8 V and the deposition time is 270 s. For sensing studies, **FMS-TA-ATT/GCE** was used as the sensing platform.

Actual sample analysis

To verify the application of the **FMS-TA-ATT/GCE** probe in a practical environment, three real water samples were collected from (a) Kalisayar Pond attached to Kalisayar Temple, a local waterbody close to Visva-Bharati University (Location: Bolpur, Birbhum, West Bengal; 23.668348° N, 87.667784° E), (b) Hoogly River, the westernmost distributary of the Ganges (Location: Katwa, Burdwan, West Bengal; 23.650682° N, 88.137188° E) and (c) Chilika Lake, a lagoon in India that is the largest brackish water lagoon in Asia and second largest coastal lagoon in the world (Location: Chilika, Odisha; 19.665469° N, 85.216650° E). The sensing studies of **FMS-TA-ATT/GCE** toward Pb^{2+} and Hg^{2+} in these samples were carried out by DPV through the variation of the concentrations of the metal ions added externally, directly with the as-collected water without using any acetate buffer.

Results and discussion

In this study, **FMS-TA-ATT** has been synthesized following the reaction route depicted in Scheme 1. For this, mesoporous silica (**MS**) with low electrical conductivity was chosen as the solid support because of its high adsorption capacity and presence of surface silanol groups that can be easily silylated with organosilanes. In the first step, **MS** has been synthesized following the standard procedure[32] and then functionalized with 3-APTES where the ethoxy groups of the latter react with the surface silanol groups of **MS** to give the aminopropyl functionalized material, **FMS**. To detect metal ions, the presence of electron-rich heteroatoms in the probe is desirable, which can bind to electron deficient metal ions. These heteroatoms can donate their lone pair of electrons to the vacant orbitals of the metal ions to form coordinate covalent bonds. Thus, in the next step, a Schiff-base condensation reaction has been performed between **FMS** and the previously prepared tris-(4-formyl phenyl) amine (**TA**). Here the mole ratio of **FMS** to tris-(4-formyl phenyl) amine is maintained in such a way that the free amine group of **FMS** undergoes condensation with only one of the three formyl groups of tris-(4-formyl phenyl) amine. After completion of this reaction, **FMS-TA** is obtained, which contains two free formyl groups and can be utilized for further functionalization to introduce more donor sites to bind the metal ions. The presence of a soft donor centre like sulphur in the probe along with other heteroatoms like oxygen and nitrogen facilitates the coordination with heavy metal ions like Pb^{2+} and Hg^{2+}. Therefore, in the final step, 5-amino-1,3,4-thiadiazole-2-thiol has been used to functionalize the two residual formyl groups of tris-(4-formyl phenyl) amine by another Schiff-base condensation to synthesize **FMS-TA-ATT**. The primary target here is to functionalize the mesoporous silica support and incorporate an ample number of N and S-donor sites into the framework. This leads to better electron transport throughout the system due to extended conjugation, which will enhance the electrical conductivity as well as introduce sensing properties in the material towards heavy metal

ions like Pb^{2+} and Hg^{2+} which prefer to bind to N and S-donor centres present in the probe. To ensure the successive functionalization in each step, it is necessary to perform the following characterization studies to optimize the changes in their physical and electrochemical properties after each modification.

The powder X-ray diffraction patterns of the samples at various stages of the synthesis are shown in Fig. 1. The appearance of three distinct diffraction peaks corresponding to (100), (110) and (200) planes suggests that the samples exhibit a 2D-ordered hexagonal mesostructure.[34] With successive functionalization of **MS** with 3-APTES (**FMS**), trialdehyde (**FMS-TA**) and 5-amino-1,3,4-thiadiazole-2-thiol (**FMS-TA-ATT**), the ordering of pores are affected to some extent which is evident from the lowering of the peak intensity. Along with this, the shifting of the peak positions to higher 2θ values is observed in Fig. 1a–d, suggesting a decrease in the *d*-spacing value in sequential functionalization.[35] The shifting of the peaks to higher 2θ values in the XRD patterns may be attributed to the condensation within the pore walls, induced by the refluxing procedure that is accompanied in each step of functionalization. The *d*-spacing values were calculated for all the materials using Bragg's law from the 2θ values corresponding to the (100) plane and are given in Table 1.

The scanning and transmission electron microscopy images of the silica support, **MS**, are presented in Fig. 2. It is evident from the scanning electron microscopy image (Fig. 2a) that **MS** contains 1D cylindrical channels throughout the entire area of the sample under observation. A more magnified image of the sample observed through transmission electron microscopy is given in Fig. 2b. It shows a small fragment of the 1D cylindrical channel of **MS** having an ordered combed structure. The image supports that the morphology is in agreement with that obtained from the FE-SEM studies. A selected

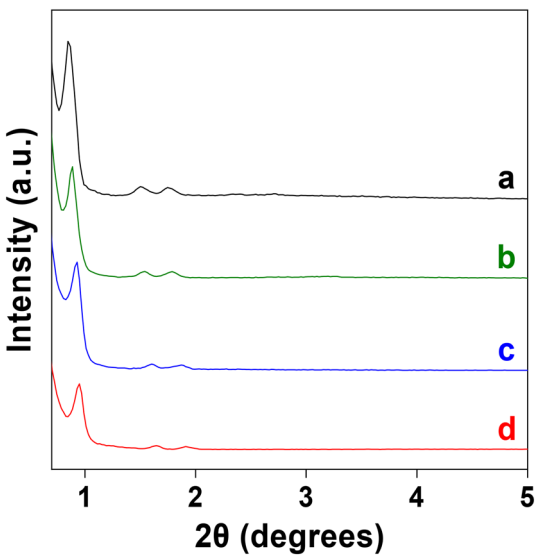

Fig. 1 Powder X-ray diffraction patterns of (a) **MS**, (b) **FMS**, (c) **FMS-TA** and (d) **FMS-TA-ATT**.

Table 1 *d*-Spacing, surface area, pore size and pore volume of different samples

Sl. no.	Sample name	*d*-Spacing in nm (from PXRD)	Surface area (m^2 g^{-1})	Pore width (nm)	Pore volume (cc g^{-1})
1	**MS**	10.34	639	7.0	0.762
2	**FMS**	9.99	265	6.8	0.528
3	**FMS-TA**	9.54	179	4.9	0.353
4	**FMS-TA-ATT**	9.31	44	5.6	0.130

area towards the end of the cylindrical channel has been magnified (inset of Fig. 2b) to view the ordered arrangement of the hexagonal mesopores with a diameter of *ca.* 8 nm. The FE-SEM image, elemental mapping and elemental content obtained from energy dispersive X-ray spectroscopy (EDS) and FE-SEM studies of **FMS-TA-ATT** are given in Fig. S1. It can be observed from Fig. S1a that 1D cylindrical channels are retained throughout the sample suggesting that no morphological change occurs due to functionalization. From the elemental mapping depicted in Fig. S1b to S1f and the atomic percentage of the elements present in the material given in Fig. S1g, it can be observed that the distributions of silicon, oxygen, carbon, nitrogen and sulphur are homogeneous and in appropriate proportion as anticipated. The atomic percentage of sulphur has been found to be *ca.* 1.18%, indicating the incorporation of the 5-amino-1,3,4-thiadiazole-2-thiol moiety in the material.

To investigate the changes in the porosity and physical properties on the surface of the materials upon functionalization, all the samples were studied for their nitrogen adsorption/desorption characteristics. The isotherms of all the materials are shown in Fig. 3. It is conclusive that all the isotherms show a type IVa pattern typical of mesoporous materials with a steep rise due to capillary condensation at a higher pressure, indicating the presence of larger mesopores.[36] Apart from this, all the materials exhibit an H1 type hysteresis loop signifying that capillary condensation occurs within uniform pores[37] and the presence of 1D cylindrical channels that confine the nitrogen molecules.[38] Though all the materials have similar kinds of isotherms, adsorption of gas decreases and the height of the hysteresis loop decreases as the mesoporous silica (**MS**) is functionalized in every successive step. From this observation, it can be concluded that the pores become narrower in each successive step of functionalization, due to which the pore volume as well as the specific surface area decreases in every step. The NLDFT pore size distributions of all the samples are provided in Fig. S2. It is evident from the distribution patterns that all the samples contain pores in the mesoporous region (4.9–7.0 nm). The initial mesoporous SBA-15 type silica support (**MS**) shows a hierarchical porosity with the presence of smaller pores of *ca.* 1.6 nm. However, upon functionalization, the smaller pores disappear and the bigger mesopores get filled with organic functionalities leading to the reduction of the pore diameters. The BET surface area, pore volume and pore size of all the samples are given in Table 1. The pore

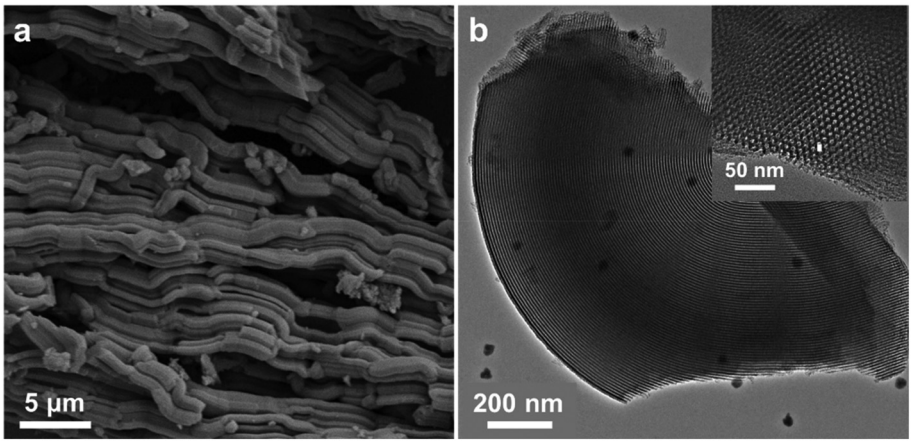

Fig. 2 (a) Scanning and (b) transmission electron microscopy images of the silica support, **MS**.

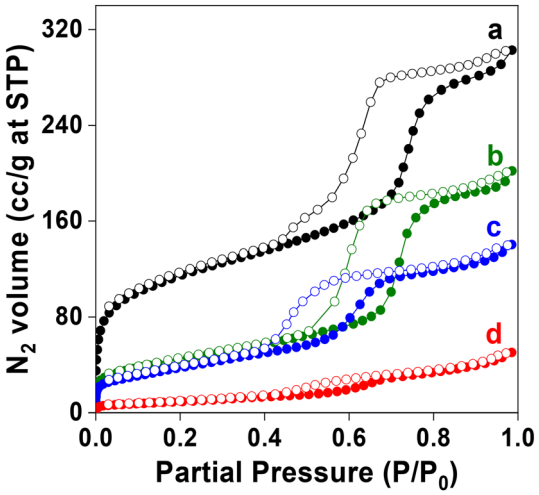

Fig. 3 Nitrogen adsorption/desorption isotherms of (a) **MS**, (b) **FMS**, (c) **FMS-TA** and (d) **FMS-TA-ATT**.

width of **MS** that is obtained using the NLDFT calculation from the adsorption isotherm of the nitrogen adsorption/desorption experiments gives a slightly lower value than that calculated from the TEM images. This pore size is obtained from the accessible area of the pore which reduces due to the gradual functionalization of the inner surface of the pores of the silica support with different organic moieties. It does not take into account the real pore to pore distance of the mesoporous silica framework.[39]

Thus, by the analysis of the PXRD patterns, electron microscopy images and results of the nitrogen adsorption/desorption studies, it can be summarized that the samples are mesoporous with uniform pore sizes ranging between 4.9 and 7.0 nm. The silica support is composed of 1D cylindrical channels with uniform hexagonal mesopores that form a continuous structure facilitating mass transfer. With gradual functionalization of **MS** to **FMS**, **FMS-TA** and **FMS-TA-ATT**, the surface of the mesoporous silica gets occupied by various organic moieties which leads to a steady decrease in the surface area, pore size and pore volume in every step.

The FT-IR studies of **MS**, **FMS**, **FMS-TA** and **FMS-TA-ATT** were carried out using KBr pellets prepared with the powdered samples to verify the functionalization of the mesoporous silica support in every individual step. The spectra of all the samples are shown in Fig. S3a. Strong bands at *ca.* 1052 cm^{-1} and 810 cm^{-1} appear for unfunctionalized silica, **MS**, which correspond to ν_s(Si–O) and ν_{as}(Si–O) bands, respectively, and these bands are retained in all the subsequent materials.[34] After functionalization with 3-APTES, **FMS** exhibits a broad band in the range of 3600 to 2845 cm^{-1},[22] which confirms the presence of amine and methylene groups in the material. Several significant bands arise at *ca.* 1690, 1641 and 1593 cm^{-1}, which may be attributed to the presence of C=O, C=N and C=C moieties, respectively, when tris(4-formylphenyl) amine reacts with **FMS** to yield **FMS-TA**.[40] The presence of both peaks, for the free formyl group at *ca.* 1690 cm^{-1} and the azomethine group at *ca.* 1641 cm^{-1}, suggests that not all the formyl groups were transformed into azomethine groups. As the molar ratio of **FMS** and tris(4-formylphenyl) amine has been maintained as 1 : 1 during the synthesis, it is anticipated that only one formyl group has been converted to the azomethine group after the reaction and two formyl groups remain available for further reaction. In the last step, formation of a Schiff base of **FMS-TA** with 5-amino-1,3,4-thiadiazole-2-thiol gives **FMS-TA-ATT**. In this material, the band at *ca.* 1690 cm^{-1} disappears whereas the band near 1641 cm^{-1} is retained, which confirms that all of the formyl groups were converted to azomethine groups. Another absorption band appears at 467 cm^{-1} for a sulphur group which corresponds to the ν(C–S) vibration and is absent in the plot of **FMS-TA**.[41] This also suggests that **FMS-TA** has been functionalized with 5-amino-1,3,4-thiadiazole-2-thiol in the successive step. For a better understanding, the magnified spectra of **FMS-TA** and **FMS-TA-ATT** in the range of 2000 to 1200 cm^{-1} and 510 to 410 cm^{-1} are given in Fig. S3b and S3c, respectively.

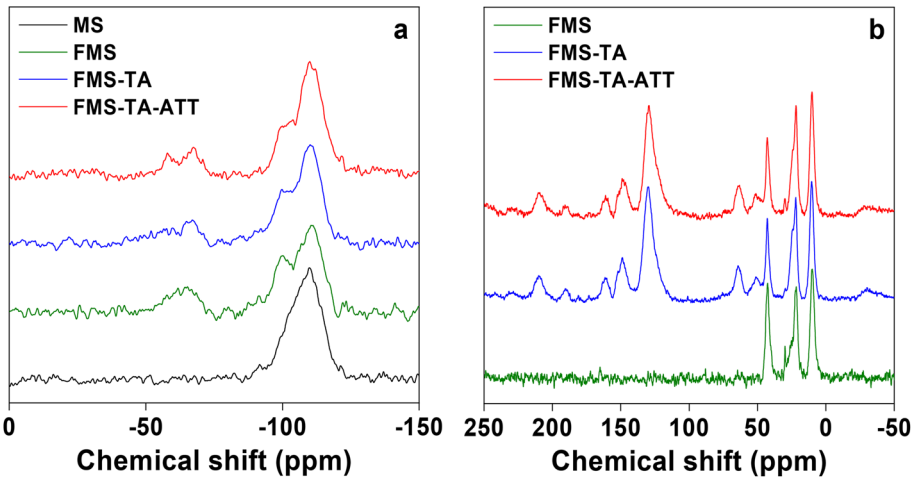

Fig. 4 (a) ^{29}Si MAS NMR spectra of **MS**, **FMS**, **FMS-TA** and **FMS-TA-ATT** and (b) ^{13}C CP MAS NMR spectra of **FMS**, **FMS-TA** and **FMS-TA-ATT**.

To understand the chemical environment around the silicon atom in the mesoporous silica samples, a study of ^{29}Si MAS NMR in the solid state has been performed. The spectra of **MS**, **FMS**, **FMS-TA** and **FMS-TA-ATT** are illustrated in Fig. 4a. For the calcined mesoporous silica support, **MS**, a peak is obtained at −109.8 ppm with a hump at −102.3 ppm. These can be attributed to the Q^4 and Q^3 centers in the silica materials, respectively, which suggest the presence of the Si $(OSi)_n(OH)_{4-n}$ units.[39] The spectra of subsequent functionalized materials, **FMS**, **FMS-TA** and **FMS-TA-ATT** are almost identical. Along with Q^4 and Q^3 centers, in the spectra of these samples, two new peaks emerge at *ca.* −65.1 ppm and −57.8 ppm due to the incorporation of the aminopropyl groups in the silica framework. The peak at around −65.1 ppm corresponds to the presence of the T^3 $((SiO)_3Si–R–Si(OSi)_3)$ species while the peak at −57.8 ppm suggests the presence of the T^2 $((HO)_2(OSi)Si–R–Si(OSi)_2(OH))$ species.[42] The similar spectral patterns of these samples indicate that the chemical environment at the silicon sites remains more or less unchanged with gradual functionalization.[35]

The structure of the materials obtained by successive incorporation of organic moieties on the silica support can be predicted from the ^{13}C CP MAS NMR spectra of the samples (except **MS**, which has no carbon containing organic counterpart), which are presented in Fig. 4b. In the spectra of the 3-APTES functionalized mesoporous silica (**FMS**), peaks appear at 10.1, 22.1 and 42.7 ppm, among which the peak at 42.7 ppm arises due to the presence of a carbon atom next to the amino group, while the peaks at 22.1 and 10.1 ppm are generated from the other two carbon atoms of the propyl chain.[35] A number of peaks appear when tris-(4-formyl phenyl) amine is incorporated into **FMS** through Schiff base condensation to obtain **FMS-TA**, thereby supporting successful functionalization. The spectrum of **FMS-TA** exhibits sharp peaks at 10.2, 22.1 and 42.9 ppm for aliphatic carbon atoms, indicating the retention of 3-APTES carbon in the framework. For the organic moieties, peaks appear at 51.1 and 64.3 ppm for the aliphatic carbons whereas the peaks at 129.9, 148.9, 190.3 and 209.6 ppm may be attributed to the aromatic carbons of the organic functional groups grafted to the silica framework. The peak at 161.2 ppm may be assigned to the azomethine group[43] and the peak at 181.3 ppm to the unreacted carbonyl carbon. These peaks confirm the formation of a Schiff base between the $–NH_2$ group of the aminopropyl moiety and the –CHO group of the tris-(4-formylphenyl) amine as well as the presence of unreacted –CHO groups in **FMS-TA**. When 5-amino-1,3,4-thiadiazole-2-thiol reacts with trialdehyde functionalized **FMS-TA** to give **FMS-TA-ATT**, the peak for the unreacted carbonyl carbon is absent, indicating that all of the free aldehyde groups have converted into the azomethine group.[44] Otherwise, the spectrum of **FMS-TA-ATT** shows all the above-mentioned peaks along with a new peak at 170.9 ppm, which may be assigned to the C–S bond of the thiadiazole moiety and thiol functional group.[45] The intensity of the peak for the C–S bond (170.9 ppm) is very low as the atomic percent of sulphur present in **FMS-TA-ATT** is only 1.18% as obtained from the EDS study of **FMS-TA-ATT**, given in Fig. S1g.

The extent of functionalization (*i.e.* % loading of organic moieties) and thermal stability of the samples in each successive step can be explained by TGA under an oxygen environment. From the weight loss plot of the samples with temperature given in Fig. S4, it can be seen that the silica support, **MS**, has high thermal stability and the total weight loss of up to 1073 K is *ca.* 5.1% only, which takes place due to the loss of adsorbed water molecules on the surface of mesoporous silica. In the next sample, **FMS**, the amount of grafting of the 3-aminopropyl triethoxysilyl group (from 3-APTES) onto mesoporous silica was found to be 12.7% and the weight loss occurred in two steps. The first weight loss of up to 393 K can be ascribed to the removal of the adsorbed water molecules and the second weight loss, at a higher temperature region, occurs due to the combustion of organic moieties grafted on the silica framework. Therefore, the estimated loading of 3-APTES on the silica framework is *ca.* 1.47 mmol g^{-1} which corresponds

to nearly 8.1% silylation. The TGA plot of **FMS-TA** obtained by the functionalization of **FMS** with tris-(4-formyl)triphenyl amine also exhibits weight loss in two distinct steps, *viz.* due to the removal of adsorbed moisture and grafted organic moieties, respectively. Its additional weight loss of *ca.* 10.14%, with respect to **FMS**, can be ascribed to the successive loading of tris-(4-formyl)triphenyl amine, which corresponds to *ca.* 0.31 mmol g^{-1}. In the final step, the incorporation of 5-amino-1,3,4-thiadiazole-2-thiol in **FMS-TA-ATT** has been calculated to be *ca.* 4.23% from the TGA plot, which is equivalent to *ca.* 0.32 mmol g^{-1}. Though the loading amount in **FMS-TA-ATT** may be expected to be twice the amount of tris-(4-formyl)triphenyl amine in **FMS-TA**, due to the removal of some amount of tris-(4-formyl)triphenyl amine during the synthesis of **FMS-TA-ATT**, the loading amount becomes somewhat less. The removal of tris-(4-formyl)triphenyl amine could be observed from the yellow color of the filtrate collected during the separation of **FMS-TA-ATT** from the reaction mixture. However, the absence of the peak for the free –CHO group in the ^{13}C MAS NMR spectra of **FMS-TA-ATT** confirmed that all the –CHO groups present in **FMS-TA** reacted with 5-amino-1,3,4-thiadiazole-2-thiol and converted into azomethine moieties. This has also been confirmed from the FT-IR spectrum.

Electrochemical studies

Cyclic voltammograms were run to assess the electrochemical behavior of the electrodes, **MS/GCE**, **FMS/GCE**, **FMS-TA/GCE** and **FMS-TA-ATT/GCE** employing $[Fe(CN)_6]^{3-/4-}$ as a redox probe. Measurements were conducted using a three-electrode setup within a working potential range of −1 to +1.1 V. Cyclic voltammograms (CVs) for all the samples were recorded at a scan rate of 5 mV s^{-1}, and the results are shown in Fig. 5. **FMS-TA-ATT/GCE** demonstrated superior performance among all electrodes, as evidenced by the greater area under its CV curve. In comparison, the other electrodes exhibited reduced redox peak currents, attributed to the poor conductivity of the materials, which impeded the electron transfer pathway on the electrode surface. Conversely, **FMS-TA-ATT/GCE** showed prominent redox peaks, indicating enhanced electron transfer facilitated by the high conductivity of the **FMS-TA-ATT** material due to the presence of sulphur along with a number of nitrogen atoms as heteroatoms. This high conductivity promoted the adsorption and electron transfer of $[Fe(CN)_6]^{3-/4-}$ on the electrode surface, thereby enhancing the overall conductivity which is also verified by the ratio of the oxidation peak current of **FMS-TA-ATT** to **FMS-TA**.

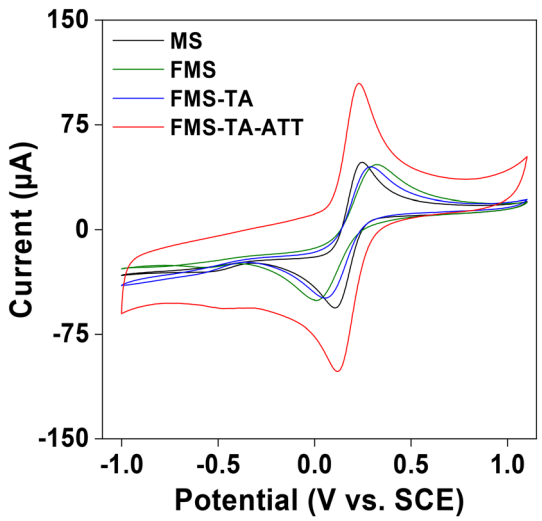

Fig. 5 Cyclic voltammograms of **MS/GCE**, **FMS/GCE**, **FMS-TA/GCE** and **FMS-TA-ATT/GCE** in 5 mM $[Fe(CN)_6]^{3-/4-}$ solution containing 0.1 M KCl at a scan rate of 5 mV s^{-1}.

The electrodes were analyzed using electrochemical impedance spectroscopy (EIS) studies in a 5 mM $[Fe(CN)_6]^{3-/4-}$ solution with a 0.1 M KCl electrolyte, within the frequency range of 10^5 Hz to 0.1 Hz. The Nyquist plots given in Fig. 6a illustrate the relationship between the $-Z''$ (imaginary) and Z' (real) impedance components of **MS/GCE**, **FMS/GCE**, **FMS-TA/GCE** and **FMS-TA-ATT/GCE**.[46] All the electrodes exhibit a similar pattern and the plots can be divided into three distinct regions. In the high-frequency region, the semi-circular portion indicates the interfacial charge transfer resistance. The slope of the mid-frequency linear region corresponds to the diffusion resistance. Finally, the nearly vertical line in the low-frequency region represents the capacitive behavior of the samples;[46] a shorter line means higher conductivity. In this case, **FMS-TA-ATT/GCE** has the shortest line confirming its higher conductivity which is also supported by the CV studies. Additionally, a smaller semicircular hump is seen in this sample at high frequency, the magnified plot of which is given in Fig. 6b, indicating its lower charge-transfer resistance at the electrode/electrolyte interface.[47] The diagram in Fig. 6c illustrates the corresponding equivalent circuit used in the measurements from the fitted EIS plot given in Fig. 6b. This circuit includes R_s (total solution resistance, contact resistance and interface resistance), charge-transfer resistance (R_{ct}), capacitance (C), contact phase element (CPE) and Warburg impedance (W).[48] The solution resistance (R_s) is connected in series with the contact phase element (CPE), charge transfer resistance (R_{ct}) and Warburg impedance (W) (where CPE is in parallel with R_{ct} and W), which are again in series with capacitance (C). R_s varies for different samples based on the contributions from total solution resistance, contact resistance and interface resistance.[49] The R_s values of **MS/GCE**, **FMS/GCE**, **FMS-TA/GCE** and **FMS-TA-ATT/GCE** obtained from the Nyquist plots are 113, 310, 58 and 170 Ω, respectively. On the other hand, the R_{ct} value of **FMS-TA-ATT/GCE** (452.0 Ω) is least in comparison with those of **MS/GCE** (13.0 kΩ), **FMS/GCE** (5.3 kΩ) or **FMS-TA/GCE** (1.4 kΩ), suggesting the fast charge transfer in the case of **FMS-TA-ATT/GCE**. Thus, based on the overall parameters of the samples, it may be concluded that **FMS-TA-ATT/GCE** exhibits the highest conductivity compared to the other functionalized samples.

In order to understand the nature of the electron transfer process, **FMS-TA-ATT/GCE** was characterized by cyclic voltammetry in 5 mM $[Fe(CN)_6]^{3-/4-}$ solution containing 0.1 M KCl.

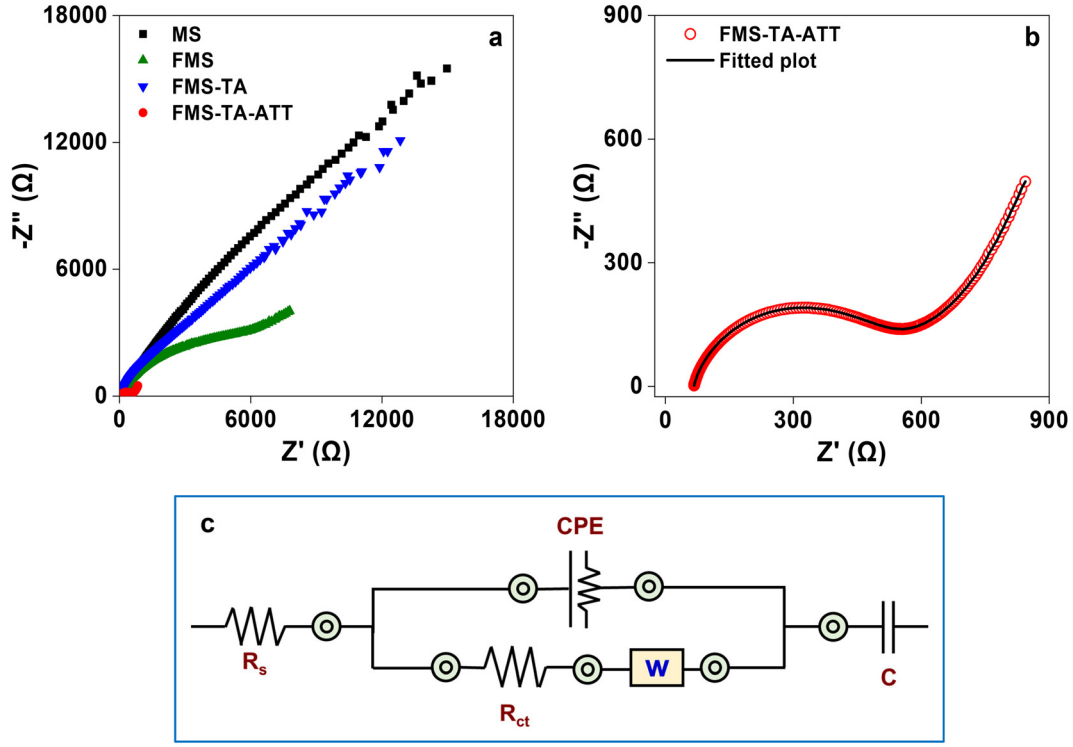

Fig. 6 (a) EIS curves of **MS/GCE**, **FMS/GCE**, **FMS-TA/GCE** and **FMS-TA-ATT/GCE** in 5 mM $[Fe(CN)_6]^{3-/4-}$ solution containing 0.1 M KCl, (b) experimental and fitted curves of **FMS-TA-ATT/GCE** and (c) diagram of the equivalent circuit for the fitted curve of **FMS-TA-ATT/GCE**.

The voltammograms were studied between the potential range of −1.0 V to +1.1 V and the scan rate range of 5 to 100 mV s^{-1}. The results of the studies are given in Fig. S5. From the data, the linear relationship between the anodic and cathodic peak currents *versus* the square root of the scan rate was plotted and the data are given in Fig. S6. From the plots, it is evident that the peak current is directly proportional to the square root of the scan rate. The linear equations of anodic (I_{pa}) and cathodic (I_{pc}) peak currents with the square root of the scan rate are given by eqn (1) and (2), respectively.

$$I_{pa}\ (\mu A) = 67.33\nu^{\frac{1}{2}} - 81.86\ (R^2 = 0.99) \quad (1)$$

$$I_{pc}\ (\mu A) = -26.90\nu^{\frac{1}{2}} - 29.52\ (R^2 = 0.99) \quad (2)$$

Apart from that, the study shows that the oxidation–reduction reaction on the surface of **FMS-TA-ATT/GCE** is a diffusion-controlled process and the current signal is enhanced due to the fast electron transfer rate.[1] The slopes obtained from eqn (1) have been used to calculate the electroactive surface area of **FMS-TA-ATT/GCE** using the Randles–Sevcik equation (eqn (3)).[50]

$$I_{pa} = 2.69 \times 10^5 \times n^{\frac{3}{2}} \times D^{\frac{1}{2}} \times A \times C \times \nu^{\frac{1}{2}} \quad (3)$$

where n, ν, C, A and D are the number of exchanged electrons (n = 1), scan rate, bulk concentration, electroactive surface area and diffusion coefficient of $[Fe(CN)_6]^{3-/4-}$ in 0.1 M KCl, respectively. The calculated electroactive surface areas are given in Table S1. It can be observed from the table that the electroactive surface area remains almost the same in the case of **MS/GCE** (0.320 cm^2), **FMS/GCE** (0.290 cm^2) and **FMS-TA/GCE** (0.275 cm^2), but it increases by almost three times in the final sample, **FMS-TA-ATT/GCE** (0.980 cm^2), reflecting an improved electrode modification.[51]

A differential pulse voltammetry (DPV) study was carried out to investigate the analytical properties of the four electrodes (**MS/GCE**, **FMS/GCE**, **FMS-TA/GCE** and **FMS-TA-ATT/GCE**) for the simultaneous detection of Pb^{2+} and Hg^{2+}. The results are shown in Fig. 7. It is observed that **FMS-TA-ATT/GCE** exhibits significantly stronger and more distinct response current peaks for the simultaneous detection of Pb^{2+} and Hg^{2+} compared to the other electrodes (Fig. 7a). It can be seen from Fig. 7a that the oxidation peak current of **FMS-TA-ATT** is twice the oxidation peak current of **FMS-TA**, which is in good agreement with the results observed from the CV studies at 5 mV s^{-1} (Fig. 5). This enhanced performance is attributed to the presence of more active sites like the thiol group, imine group, thiadiazole group, *etc.* in **FMS-TA-ATT**, which greatly increases the electroactive surface area of the sensing electrode (Table S1). The probable binding sites for metal ion coordination are shown in Scheme 2. It is anticipated that the binding of the metal ions takes place through both the N and S donor sites. However, S, being a soft center, facilitates the binding with the soft lead and mercury ions. The capability of **FMS-TA-ATT/GCE** was further analyzed for the individual and simultaneous detection of Pb^{2+} and Hg^{2+} (Fig. 7b). The results

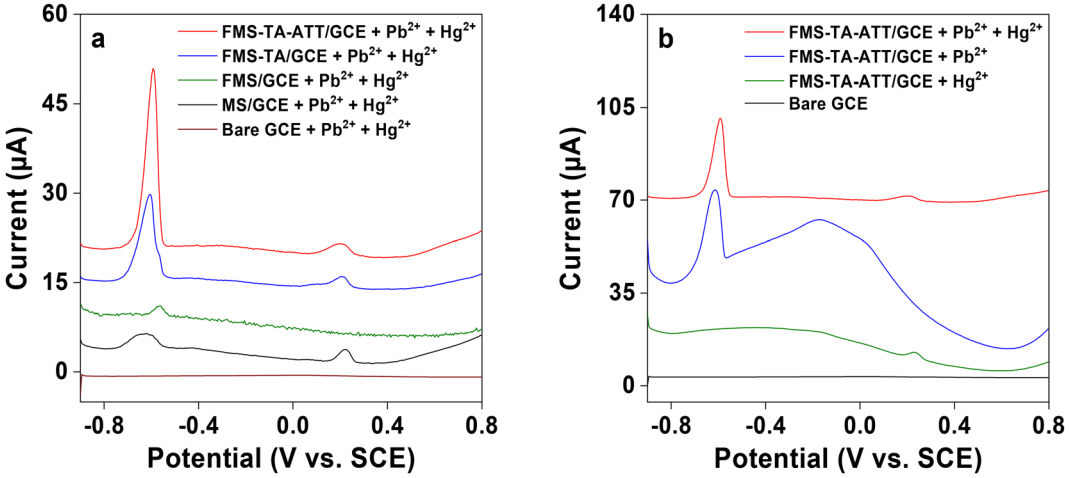

Fig. 7 Differential pulse voltammetric (DPV) curves of (a) bare GCE, **MS/GCE**, **FMS/GCE**, **FMS-TA/GCE** and **FMS-TA-ATT/GCE** for the simultaneous detection of Pb^{2+} and Hg^{2+} in 0.2 M acetate buffer solution (pH = 7) and (b) bare GCE and **FMS-TA-ATT/GCE** for both individual and simultaneous detection of Pb^{2+} and Hg^{2+} in 0.2 M acetate buffer solution (pH = 7).

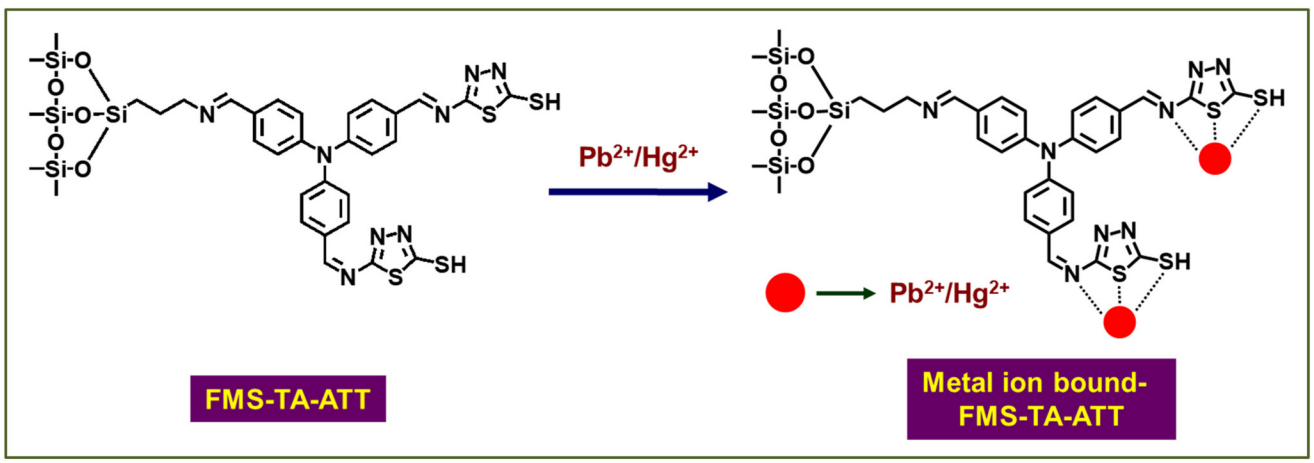

Scheme 2 Plausible mechanism of metal ion sensing by **FMS-TA-ATT**.

indicated that the electrode could detect Pb^{2+} and Hg^{2+}, both individually and simultaneously, which demonstrates its practical utility.[1] It is pertinent to mention here that when this material is used for simultaneous detection of the two metal ions, its sensing ability decreases to a small extent in terms of the output current produced.[52] In the case of individual sensing of Pb^{2+} and Hg^{2+} by **FMS-TA-ATT/GCE**, all the active sites are available to bind either Pb^{2+} or Hg^{2+}, while in simultaneous detection, active sites will be distributed to bind Pb^{2+} and Hg^{2+} at a time, leading to a small decrease in the output current at the corresponding peaks for Pb^{2+} and Hg^{2+}.

Experimental parameters such as deposition time, deposition potential and electrolyte pH, which affect the electrochemical activity, were optimized to obtain high sensitivity detection of lead and mercury ions by **FMS-TA-ATT/GCE**. The binding capacity of the surface of **FMS-TA-ATT/GCE** to the target ions was tested using the accumulation time effect. For this, several accumulation time intervals, from 60 to 300 s, were applied keeping the concentration of lead and mercury ions fixed. It can be observed from Fig. S7a that the oxidation peak gradually increases with the deposition time from 60 to 270 s. Then it progressively decreases after 270 s. This phenomenon is probably observed due to the electrostatic repulsion phenomenon after the active sites are gradually saturated. The DPV detection curves for various deposition voltages are shown in Fig. S7b. It is evident from the curves that choosing different deposition voltages leads to significant variations in the peak current. The peak current reaches its maximum when the deposition voltage is −0.8 V and therefore, −0.8 V was used in subsequent experiments. The results of the studies of the effect of electrolyte pH on the determination of Pb^{2+} and Hg^{2+} within the pH range of *ca.* 5.5 to 7.5 are presented in Fig. S7c. As shown in the figure, the highest peak currents for Pb^{2+} and Hg^{2+} were observed at pH = 7. The

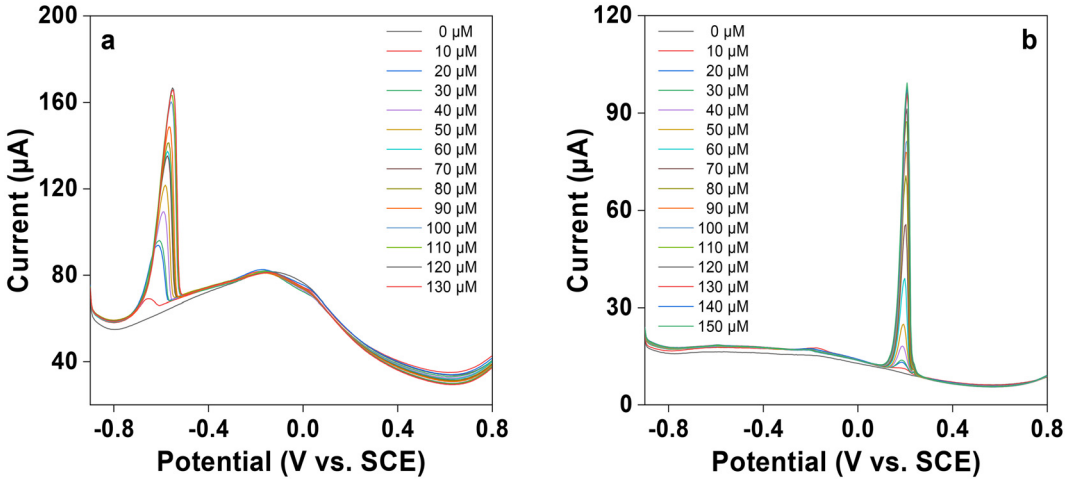

Fig. 8 DPV study of (a) Pb^{2+} and (b) Hg^{2+} sensing at different concentrations using **FMS-TA-ATT/GCE** with a deposition potential of −0.8 V and a deposition time of 270 s in 0.2 M acetate buffer solution (pH = 7).

reduction in peak current at pH levels below 7 may be attributed to the protonation of the imine and thiol groups due to the presence of a high concentration of hydrogen ions in the solution, which disrupts the current response.[53,54] However, as the pH increases, protonation is suppressed and the electroactive surface provides more unprotonated nitrogen and sulphur atoms to bind Pb^{2+} and Hg^{2+} leading to higher current responses.[55] At pH values higher than 7, a low peak current is observed, possibly due to the formation of a metal hydroxide complex.[56] Thus, the optimization conditions for the sensing of Pb^{2+} and Hg^{2+} were chosen as follows: deposition time = 270 s; deposition potential = −0.8 V and pH = 7.

Under the optimized experimental conditions, the gradual responses of Pb^{2+} and Hg^{2+} were individually investigated in 0.2 M acetate buffer solution. As depicted in Fig. 8a, the dissolution peak current gradually increases with the increase in Pb^{2+} concentration from 0 to 130 μM at a potential of *ca.* −0.55 V *vs.* SCE. In the range of 0–150 μM, an increase in current response is observed at 0.21 V *vs.* SCE with the increase in Hg^{2+} concentration, as shown in Fig. 8b. The dissolution peak current responses are plotted against the concentration of the individual metal ions and both the calibration plots are given in Fig. S8. Fig. S8a and S8b exhibit two linear concentration ranges from 0 to 50 μM and 50 to 100 μM for the detection of Pb^{2+} and 0–50 μM and 50–90 μM for the detection of Hg^{2+}, respectively. Both the calibration plots show a similar kind of adsorption pattern at the surface of the electrode. The first linear range implies slower adsorption which may happen due to the low concentration of the metal ions. The dissolution peak current is saturated at *ca.* 120 and 140 μM for Pb^{2+} and Hg^{2+}, respectively, due to the high accumulation of the metal ions at the surface of the electrode which may limit the adsorption of the ions.[57]

From the data, the sensitivity of sensing of Pb^{2+} and Hg^{2+} has been found to be (i) 0.4927 μA μM^{-1} cm^{-2} (for the 0–50 μM linear range) and 8.70 μA μM^{-1} cm^{-2} (for the 50–100 μM linear range) for Pb^{2+} and (ii) 0.709 μA μM^{-1} cm^{-2} (for the 0–50 μM linear range) and 8.199 μA μM^{-1} cm^{-2} (for the 50–90 μM linear range) for Hg^{2+}. From the second linear range, the LOD (limit of detection) and LOQ (limit of quantification) values were calculated using the following equations:[6]

$$\mathrm{LOD} = \frac{3\,\mathrm{SD}}{S} \tag{4}$$

$$\mathrm{LOQ} = \frac{10\,\mathrm{SD}}{S} \tag{5}$$

where SD is the standard deviation obtained from 10 replicate measurements of the voltammogram of **FMS-TA-ATT/GCE** in the blank solution (electrolyte solution in the absence of an analyte) shown in Fig. S9, and S is the slope of the calibration plot (current *vs.* concentration of the metal ions) given in Fig. S8. The LOD and LOQ for Pb^{2+} are 13 nM and 43 nM, respectively, in the linear range of 50–100 μM. Whereas, for Hg^{2+}, the LOD and LOQ are 29 nM and 95 nM, respectively, in the linear range of 50–90 μM. It has been noticed that the LOQ values are generally higher or equal to the LOD values as it requires both detection and quantification involving more accuracy and precision.

In addition to the individual detection of Pb^{2+} and Hg^{2+}, simultaneous detection of Pb^{2+} and Hg^{2+} has also been studied similarly using **FMS-TA-ATT/GCE** in 0.2 M acetate buffer solution and the results are shown in Fig. 9a and c. It is observed that the metal ions show well-separated voltammetric peaks, devoid of any mutual interference, with an increase in metal ion concentrations. This provides strong evidence that the modified GCE electrode can function as a reliable probe for the simultaneous and selective detection of both the metal ions co-existing in a solution. As the concentration of the metal ions increases, the dissolution peak current increases gradually. From these results it is evident that **FMS-TA-ATT** is able to sense both the metal ions individually in the presence

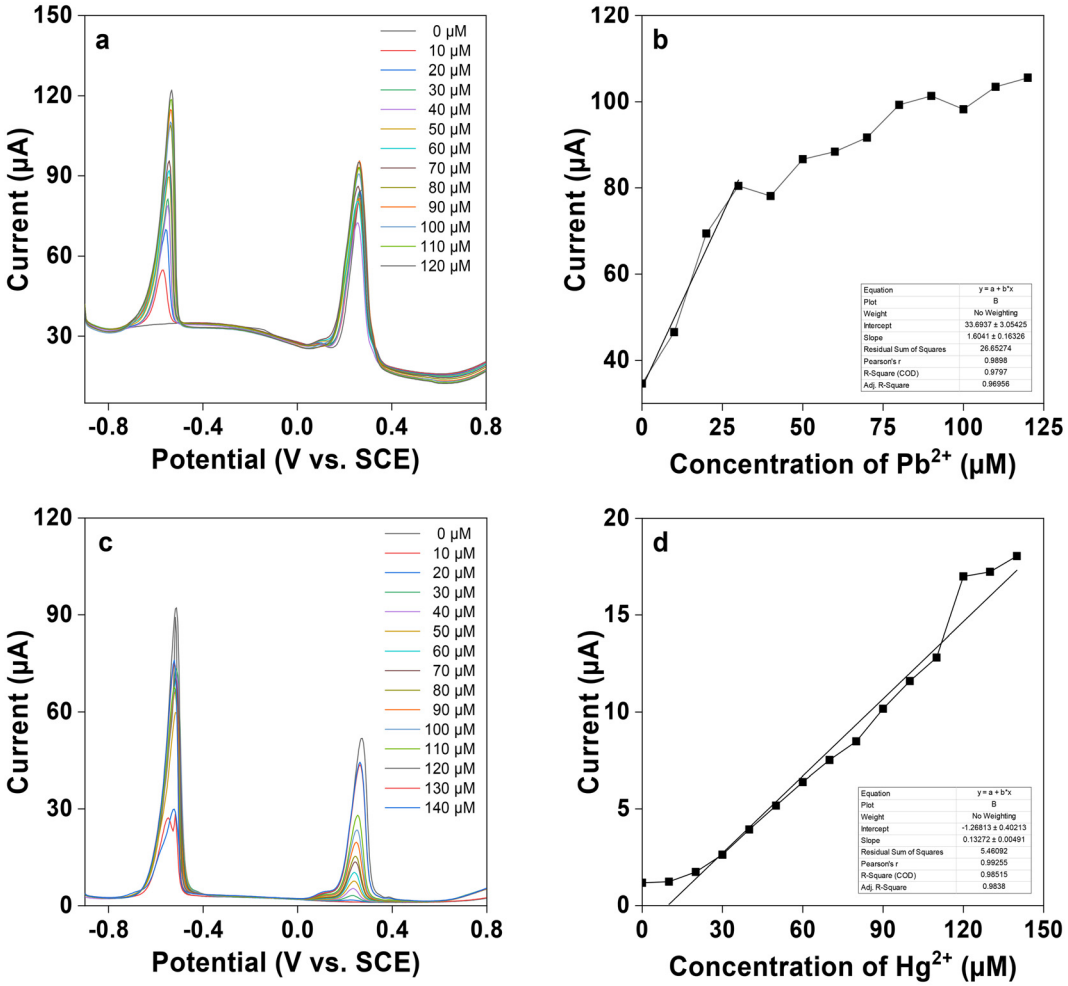

Fig. 9 (a) Detection of Pb^{2+} in the presence of Hg^{2+} by varying the concentrations of Pb^{2+} from 0 to 120 μM, (b) calibration plot for the detection of Pb^{2+} in the presence of Hg^{2+}, (c) detection of Hg^{2+} in the presence of Pb^{2+} by varying the concentrations of Hg^{2+} from 0 to 140 μM and (d) calibration plot for the detection of Hg^{2+} in the presence of Pb^{2+} in 0.2 M acetate buffer solution (pH = 7).

of other metal ions. From the calibration curves shown in Fig. 9b and d, the linear ranges are found to be 0–30 μM for Pb^{2+} and 0–140 μM for Hg^{2+}. The LOD and LOQ values are 14 nM and 46 nM for Pb^{2+}, and 185 nM and 616 nM for Hg^{2+}, respectively. The increase in the values of LOD and LOQ in simultaneous sensing *vis-à-vis* individual sensing may be explained by the fact that when multiple analytes are present in simultaneous sensing, they can compete with each other for binding to the surface of the probe. This may result in an interference in the electrochemical signals of each other leading to reduced sensitivity compared to individual sensing.[12,27] From these observations it can be stated that **FMS-TA-ATT/GCE** has good detection capability towards both the ions in the presence of other ions.

The merit of a sensor depends not only on its sensitivity and fast detection of targets but also on its ability to perform in the presence of other interferents. Thus, the interference test of **FMS-TA-ATT/GCE** has been carried out for individual sensing of both Pb^{2+} and Hg^{2+} in the presence of some common metal ions as interferents, *e.g.* Al^{3+}, Mn^{2+}, Co^{2+}, Ni^{2+}, Cu^{2+}, Zn^{2+} and Cd^{2+}. For sensing Pb^{2+}, 120 μM Al^{3+}, Mn^{2+}, Co^{2+}, Ni^{2+}, Cu^{2+}, Zn^{2+}, Cd^{2+} and Hg^{2+} were added separately to 0.2 M acetate buffer solution containing 120 μM Pb^{2+}. On the other hand, 140 μM Al^{3+}, Mn^{2+}, Co^{2+}, Ni^{2+}, Cu^{2+}, Zn^{2+}, Cd^{2+} and Pb^{2+} were added to 0.2 M acetate buffer solution containing 140 μM Hg^{2+} for sensing Hg^{2+}. The change in current responses due to such addition, recorded for Pb^{2+} and Hg^{2+}, are displayed in Fig. 10a and b, respectively. These studies indicate that **FMS-TA-ATT/GCE** has good selectivity and anti-interference ability towards sensing of Pb^{2+} and Hg^{2+} in 0.2 M acetate buffer solution.

Another important parameter of a practical sensor is illustrated by its utility in sensing applications using real samples. Thus, the sensing ability of **FMS-TA-ATT/GCE** will be useful when it can be used to sense the analytes in real water samples. For this purpose, three different sources of water (Kalisayar Pond, Hoogly River and Chilika Lake) as defined in the Experimental section were chosen. The sensing studies

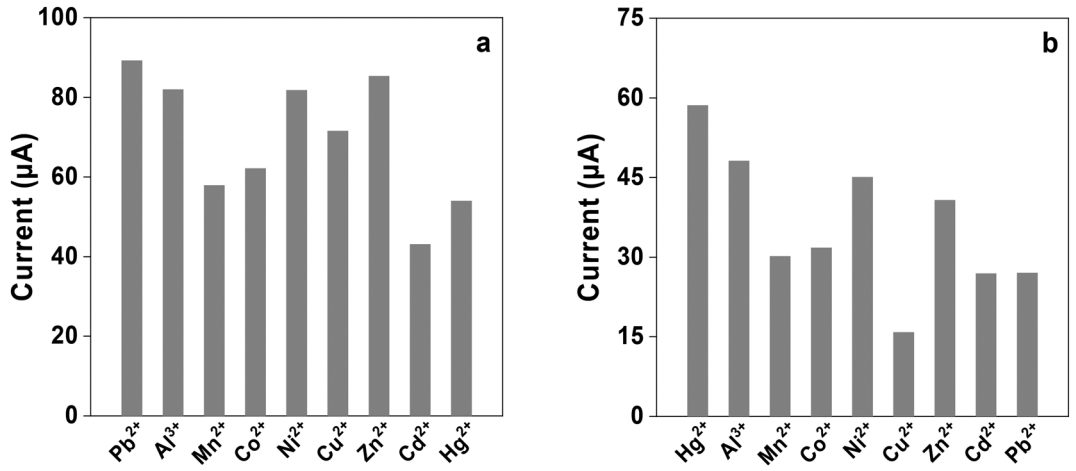

Fig. 10 Change in the oxidation peak current of **FMS-TA-ATT/GCE** for sensing (a) Pb^{2+} (120 μM) and (b) Hg^{2+} (140 μM) before and after the addition of common interfering metal ions at concentrations of 120 μM and 140 μM, respectively.

Table 2 Comparative study of **FMS-TA-ATT/GCE** with previously reported studies for the electrochemical detection of Pb^{2+} and Hg^{2+}

Sl. no.	Electrode material	Method	Electroactive analyte	Electrolyte	pH	LOD	Ref.
1	Gold nanoparticle-modified carbon thread	DPV	Cd^{2+}, Pb^{2+}, Cu^{2+} and Hg^{2+}	HCl/KCl buffer	2.0	0.99, 0.62 μM, 1.38 and 0.72 μM	59
2	OL-MBene (open-layered 2D transition metal borides)	SWASV[a]	Cd^{2+}, Pb^{2+}, Cu^{2+} and Hg^{2+}	—	4.0	0.112, 0.0481, 0.0495 and 0.0678 μM	28
3	5-BHAHS@NC/MnO_2 [(*E*)-4-((5-bromo-2-hydroxybenzylidene) amino)-3-hydroxynaphthalene-1-sulfonic acid (5-BHAHS)/nano-cellulose/MnO_2 nanoparticles]	DPV	Hg^{2+}, Cd^{2+} and Pb^{2+}	0.1 M HNO_3	6.0	0.12, 0.12 and 0.03 μM	60
4	SDA/MWCNTs (*N*,*N*′-bis(salicylaldehyde)-1,2-diaminobenzene/MWCNT)	SWASV	Hg^{2+}	0.1 M $NaNO_3$	5.0	0.24 μg L^{-1}	61
5	Co@NC/MWCNT/GCE (ZIF-67-derived cobalt/nitrogen-doped carbon composite polyhedra linked with multiwalled carbon nanotubes)	SWSV[b]	Cd^{2+} and Pb^{2+}	0.2 M NaAc/HAc buffer	5.6	4.50 and 4.90 nM	1
6	AuNP/0.75% APTES-ITO (indium tin oxide electrodes functionalized with 3-aminopropyl triethoxysilane/as-synthesized gold nanoparticle assembly)	SWASV	Cd^{2+}, Pb^{2+} and Cu^{2+}	0.2 M NaAc/HAc buffer	4.5	0.73, 0.90 and 0.49 ppb	62
7	IONP-COOH/APTES-ITO (carboxyl-stabilized iron oxide nanoparticles/3-aminopropyl triethoxysilane functionalized indium tin oxide)	SWASV	Cd^{2+} and Pb^{2+}	0.1 M NaAc/HAc buffer	4.5	0.90 and 0.60 ppb	63
8	GQDTU-IIP-GCE (ion imprinted polymer of the thiourea derivative functionalised graphene quantum dot modified glassy carbon electrode)	CV and DPV	Hg^{2+}	NaAc/HAc buffer	5.0	23.5 nM	64
9	S-g-C_3N_4/GCE (sulphur-doped graphitic carbon nitride nanoflakes)	DPV	Pb^{2+}	0.2 M NaAc/HAc buffer	4.4	3.0×10^{-9} mol L^{-1}	65
10	Alk-Ti_3C_2/GCE (alkalization-intercalated Ti_3C_2)	SWASV	Cd^{2+}, Pb^{2+}, Cu^{2+} and Hg^{2+}	0.1 M NaAc/HAc buffer	5.0	0.098, 0.041, 0.032 and 0.130 μM	66
11	$Pd_{1.5}$/PAC-900-modified GCE (palladium nanoparticles on porous activated carbon)	DPV	Cd^{2+}, Pb^{2+}, Cu^{2+} and Hg^{2+}	0.1 M NaAc/HAc buffer	5.0	41, 50, 66 and 54 nM	52
12	Nafion-HAP/GCE (composite of hydroxyapatite/Nafion)	DPASV[c]	Hg^{2+}, Cu^{2+}, Pb^{2+} and Cd^{2+}	0.1 M NaAc/HAc buffer	3.0	0.030, 0.021, 0.049 and 0.035 μM	67
13	Au-DMAET-(SWCNT-PABS) (single walled carbon nanotube-poly(*m*-amino benzene sulfonic acid) attached on a gold electrode surface)	SWASV	Hg^{2+}	0.1 M HCl	3.0	0.06 μM	68
14	**FMS-TA-ATT/GCE**	DPV	$Pb^{2+}$and Hg^{2+}	0.2 M NaAc/HAc buffer	7.0	13 and 29 nM (0.013 and 0.029 μM)	Present work

[a] Square wave anodic stripping voltammetry. [b] Square wave stripping voltammetry. [c] Differential pulse anodic stripping voltammetry.

were carried out without adding any buffer or electrolyte solution as it has already been established that **FMS-TA-ATT/GCE** is able to detect Pb^{2+} and Hg^{2+} at nearly neutral pH. It is interesting to observe that the electrode retains its sensing ability in these real water samples. For the water from the Kalisayar Pond, the sensing ability of the electrode saturates at a concentration of 100 μM of both the ions, which is illustrated in Fig. S10. In the case of the water from Hoogly River, the saturation of sensing occurs at 150 μM of both the ions (Fig. S11) and for the water collected from Chilika Lake, the saturation occurs at 50 μM (Fig. S12). The decrease in sensitivity of **FMS-TA-ATT/GCE** towards the detection of Pb^{2+} and Hg^{2+} in real water samples may be attributed to the presence of interfering substances and the variation of the pH values of these water samples. Real water samples may contain different types of ions, pollutants and compounds which can interfere during the detection of the target analyte by the probe, resulting in a lowering of the sensing ability.[58] Moreover, in the present study the sensing of Pb^{2+} and Hg^{2+} is pH dependent and all the real water samples have different pH values, *viz.* the pH of water from Kalisayar Pond is 6.8, that from Hoogly River is 8.5 and that from Chilika Lake is 7.9. These two reasons are primarily responsible for the lower sensitivity towards the sensing of the metal ions using real water samples. Thus, from these results it can be concluded that electrodes fabricated from **FMS-TA-ATT** can be used in any industrial or geological survey to detect the presence of Pb^{2+} and Hg^{2+} in any aqueous sample.

Comparative data for both individual and simultaneous detection of Pb^{2+} and Hg^{2+} are enlisted in Table 2,[1,28,52,59–68] mentioning all the required data including the type of material, the detection technique, the supporting electrolyte, the pH and the LOD of all the detectable metal ions by the respective electrode material. Analyzing all the LOD values for Pb^{2+} and Hg^{2+}, it is found that **FMS-TA-ATT/GCE** has comparable sensitivity towards the detection of these toxic metal ions (Pb^{2+} and Hg^{2+}) in neutral aqueous medium, whereas the other materials show sensitivity towards the metal ions in acidic medium generally. As neutral medium is biologically and environmentally more relevant, **FMS-TA-ATT/GCE** can be useful to detect both the metal ions with a practical impact. Along with this, it is found that the LOD values for sensing Pb^{2+} and Hg^{2+} (13 nM and 29 nM, respectively) using **FMS-TA-ATT/GCE** in this work are lower than the LOD values mentioned in the recent reports for both the metal ions.[28,59,60] On the basis of these data, it can be stated that **FMS-TA-ATT** can be used effectively to detect trace amounts of Pb^{2+} and Hg^{2+} in neutral aqueous medium in comparison to several other materials.

Conclusions

Metal ion pollution is one of the most threatening problems as it is very difficult to eliminate these ions once they enter the food chain by some means. To deal with this problem, efficient detection and quantification of metal ions in the environment from various sources is very important. In this regard, sensing of heavy metals like Pb^{2+} and Hg^{2+} occupies a prominent position due to their highly toxic nature. For this purpose, a silica-based thiol-functionalized sensor, **FMS-TA-ATT**, has been synthesized, which is capable of electrochemically sensing Pb^{2+} and Hg^{2+} in 0.2 M acetate buffer solution and thereby exhibits good detection ability in neutral medium (pH = 7). The physical properties of the material and its chemical structure were established by various characterization techniques. Electrochemical studies carried out with the sample coated over a glassy carbon electrode (**FMS-TA-ATT/GCE**) indicated that the material is capable of selectively sensing lead and mercury ions, both individually and simultaneously. The sensing study of **FMS-TA-ATT/GCE** examined by differential pulse voltammetry showed good selectivity and sensitivity towards Pb^{2+} and Hg^{2+} at pH = 7 in 0.2 M acetate buffer solution. The limits of detection as low as 13 nM for Pb^{2+} and 29 nM for Hg^{2+} could be reached. Additionally, the probe is also very efficient at detecting these two heavy metal ions in the presence of other common metal ions. As **FMS-TA-ATT/GCE** is capable of sensing Pb^{2+} and Hg^{2+} in neutral aqueous medium (pH = 7), its sensing ability was studied using real water samples collected from local water bodies as well as distant places. It was found that the material could sense the ions in these water samples too. Thus, from the present study, it may be concluded that **FMS-TA-ATT** acts as an effective electrochemical sensor and can detect Pb^{2+} and Hg^{2+} individually and simultaneously, serving as a good probe in heavy metal detection in aqueous samples.

Conflicts of interest

The authors declare no conflicts of interest.

Data availability

The data supporting this article have been included as part of the SI.

Supplementary information is available. See DOI: **https://doi.org/10.1039/d5dt01618e**.

Acknowledgements

MN gratefully acknowledges financial support from the CSIR, New Delhi (sanction letter no. 01(3088)/21/EMR-II). BS wishes to thank the UGC-NFOBC, New Delhi, for providing a fellowship. The authors acknowledge the DST-FIST Program of Integrated Science Education and Research Centre, Visva-Bharati and the DST-PURSE Project, Visva-Bharati, for providing instrumental facilities.

References

1 J. Zhao, Y. Long, C. He, H. Yang, S. Zhao, X. Luo, D. Huo and C. Hou, *ACS Sustainable Chem. Eng.*, 2023, **11**, 2160–2171.
2 F. Rechotnek, H. D. M. Follmann and R. Silva, *J. Environ. Chem. Eng.*, 2021, **9**, 106492.
3 D. Peng, L. Zhang, R.-P. Liang and J.-D. Qiu, *ACS Sens.*, 2018, **3**, 1040–1047.
4 H. Wang, L. Yang, S. Chu, B. Liu, Q. Zhang, L. Zou, S. Yu and C. Jiang, *Anal. Chem.*, 2019, **91**, 9292–9299.
5 A. Hasan, N. M. Q. Nanakali, A. Salihi, B. Rasti, M. Sharifi, F. Attar, H. Derakhshankhah, I. A. Mustafa, S. Z. Abdulqadir and M. Falahati, *Talanta*, 2020, **215**, 120939.
6 T. Kokab, A. Shah, F. J. Iftikhar, J. Nisar, M. S. Akhter and S. B. Khan, *ACS Omega*, 2019, **4**, 22057–22068.
7 L. Wang, X. Peng, H. Fu, C. Huang, Y. Li and Z. Liu, *Biosens. Bioelectron.*, 2020, **147**, 111777.
8 J. Lin, N. Chen, R. Feng, M. J. Nilges, Y. Jia, S. Wang and Y. Pan, *Environ. Sci. Technol.*, 2020, **54**, 3169–3180.
9 A. Hong, Q. Tang, A. U. Khan, M. Miao, Z. Xu, F. Dang, Q. Liu, Y. Wang, D. Lin, J. Filser and L. Li, *Anal. Chem.*, 2021, **93**, 1962–1968.
10 S. Bari, D. Maity, D. Mridha, T. Roychowdhury, P. Ghosh and P. Roy, *Anal. Methods*, 2024, **16**, 5642–5651.
11 V. Dhinakaran, K. Vigneswari, M. Lavanya and M. V. Shree, *Compr. Anal. Chem.*, 2020, **91**, 235–262.
12 R. Hu, X. Zhang, K.-N. Chi, T. Yang and Y.-H. Yang, *ACS Appl. Mater. Interfaces*, 2020, **12**, 30770–30778.
13 S. Singh, A. Numan, M. Khalid, I. Bello, E. Panza and S. Cinti, *Small*, 2023, **19**, 2208209.
14 T. A. Tabish, Y. Zhu, S. Shukla, S. Kadian, G. S. Sangha, C. A. Lygate and R. J. Narayan, *Appl. Phys. Rev.*, 2023, **10**, 041310.
15 S. Masrat, V. Nagal, M. Khan, A. Ahmad, M. B. Alshammari, S. Alam, U. T. Nakate, B. Lee, P. Mishra, K. S. Bhat and R. Ahmad, *ACS Appl. Nano Mater.*, 2023, **6**, 16615–16624.
16 B. Kashyap and R. Kumar, *Biosens. Bioelectron.*, 2022, **216**, 114628.
17 L. Zhang, Y. Pu, W. Xu, J. Peng, Y. Liu and H. Du, *Microchem. J.*, 2024, **201**, 110542.
18 L. W. Tang, Y. Alias and P. M. Woi, *J. Electroanal. Chem.*, 2024, **967**, 118427.
19 A. Dhaffouli, P. A. Salazar-Carballo, S. Carinelli, M. Holzinger and H. Barhoumi, *Mater. Chem. Phys.*, 2024, **318**, 129253.
20 T. Das, R. Chatterjee, A. Majee, H. Uyama, D. Morgan and M. Nandi, *Dalton Trans.*, 2019, **48**, 17874–17886.
21 M. Nandi, M. Sarkar, K. Sarkar and A. Bhaumik, *J. Phys. Chem. C*, 2009, **113**, 6839–6844.
22 T. Das, D. Singha, A. Pal and M. Nandi, *Sci. Rep.*, 2019, **9**, 19378.
23 A. Walcarius, *Electroanalysis*, 1998, **10**, 1217–1235.
24 L. Cui, J. Wu and H. Ju, *Biosens. Bioelectron.*, 2015, **63**, 276–286.
25 A.-M. Sacara, F. Pitzalis, A. Salis, G. L. Turdean and L. M. Muresan, *ACS Omega*, 2019, **4**, 1410–1415.
26 X. Li, W. Ma, H. Li, Q. Zhang and H. Liu, *Coord. Chem. Rev.*, 2020, **408**, 213191.
27 F.-F. Wang, C. Liu, J. Yang, H.-L. Xu, W.-Y. Pei and J.-F. Ma, *Chem. Eng. J.*, 2022, **438**, 135639.
28 S. Wei, G. Kale and X. Lai, *Sens. Actuators, B*, 2025, **429**, 137258.
29 P. Keerthana, A. George, M. Bharath, M. Ghosh and A. Varghese, *Chem. Eng. J.*, 2024, **480**, 148018.
30 D. D. Perrin, W. L. F. Armarego and D. R. Perrin, *Pergamon Press*, Oxford, U.K., 1980.
31 P. Pal, A. Pal, M. Pal and M. Nandi, *ACS Appl. Nano Mater.*, 2024, **7**, 22975–22988.
32 D. Zhao, J. Feng, Q. Huo, N. Melosh, G. H. Fredrickson, B. F. Chmelka and G. D. Stucky, *Science*, 1998, **279**, 548–542.
33 T. Mallegol, S. Gmouh, M. A. A. Meziane, M. Blanchard-Desce and O. Mongin, *Synthesis*, 2005, 1771–1774.
34 D. Singha, A. Pal, P. Roy and M. Nandi, *Eur. J. Inorg. Chem.*, 2022, e202101103.
35 T. Das, D. Singha and M. Nandi, *Dalton Trans.*, 2020, **49**, 10138–10155.
36 M. Thommes, K. Kaneko, A. V. Neimark, J. P. Olivier, F. Rodriguez-Reinoso, J. Rouquerol and K. S. W. Sing, *Pure Appl. Chem.*, 2015, **87**, 1051–1069.
37 P. Zarabadi-Poor, A. Badiei, A. A. Yousefi and J. Barroso-Flores, *J. Phys. Chem. C*, 2013, **117**, 9281–9289.
38 A. Grosman and C. Ortega, *Langmuir*, 2005, **21**, 10515–10521.
39 D. Singha, A. Pal, H. Uyama, P. Roy and M. Nandi, *Dalton Trans.*, 2021, **50**, 12478–12494.
40 B. Saha, D. Singha, T. Das and M. Nandi, *Inorg. Chim. Acta*, 2023, **550**, 121455.
41 P. Ratha, L. Chitra, I. Ancy, P. Kumaradhas and T. Palvannan, *Biochimie*, 2017, **138**, 70–81.
42 S. Inagaki, S. Guan, Y. Fukushima, T. Ohsuna and O. Terasaki, *J. Am. Chem. Soc.*, 1999, **121**, 9611–9614.
43 P. A. Sobarzo, C. A. Terraza and E. M. Maya, *Eur. Polym. J.*, 2020, **126**, 109567.
44 D. Singha, T. Das, L. Satyanarayana, P. Roy and M. Nandi, *New J. Chem.*, 2019, **43**, 15563–15574.
45 D. Pakulski, V. Montes-García, A. Gorczyński, W. Czepa, T. Chudziak, P. Samorì and A. Ciesielski, *J. Mater. Chem. A*, 2022, **10**, 16685–16696.
46 A. Pal, M. Pal, S. Ghosh and M. Nandi, *Energy Fuels*, 2022, **36**, 12285–12298.
47 M. Pal, A. Pal, P. Pal and M. Nandi, *ACS Appl. Eng. Mater.*, 2023, **1**, 2965–2983.
48 M. Pal, S. Bhowmik and M. Nandi, *New J. Chem.*, 2024, **48**, 16931–16947.
49 P. Pal, S. Bhowmik and M. Nandi, *Chem. – Eur. J.*, 2024, **30**, e202400638.

50 D. Salinas-Torres, F. Huerta, F. Montilla and E. Morallón, *Electrochim. Acta*, 2011, **56**, 2464–2470.
51 D. S. B. Ali, F. Krid, M. Nacef, E. H. Boussaha, M. L. Chelaghmia, H. Tabet, R. Selaimia, A. Atamnia and A. M. Affoune, *RSC Adv.*, 2023, **13**, 18734–18747.
52 P. Veerakumar, V. Veeramani, S.-M. Chen, R. Madhu and S.-B. Liu, *ACS Appl. Mater. Interfaces*, 2016, **8**, 1319–1326.
53 Y. Li, R. Cui, H. Huang, J. Dong, B. Liu, D. Zhao, J. Wang, D. Wang, H. Yuan, X. Guo and B. Sun, *Anal. Chim. Acta*, 2020, **1125**, 76–85.
54 Y. Li, H. Huang, R. Cui, D. Wang, Z. Yin, D. Wang, L. Zheng, J. Zhang, Y. Zhao, H. Yuan, J. Dong, X. Guo and B. Sun, *Sens. Actuators, B*, 2021, **332**, 129519.
55 F. S. Awad, K. M. AbouZeid, W. M. A. El-Maaty, A. M. El-Wakil and M. S. El-Shall, *ACS Appl. Mater. Interfaces*, 2017, **9**, 34230–34242.
56 X. Zhu, B. Liu, S. Chen, L. Wu, J. Yang, S. Liang, K. Xiao, J. Hu and H. Hou, *J. Electrochem. Soc.*, 2020, **167**, 087505.
57 N. Karikalan, R. Karthik, S.-M. Chen, C. Karuppiah and A. Elangovan, *Sci. Rep.*, 2017, **7**, 2494.
58 D. Wu, Y. Hu, H. Cheng and X. Ye, *Molecules*, 2023, **28**, 3601.
59 S. A. Lahari, N. Kumawat, K. Amreen, R. N. Ponnalagu and S. Goel, *npj Clean Water*, 2025, **8**, 10.
60 A. E. Sikaily, D. G. Ghoniem, O. Ramadan, E. M. El-Nahrery, A. Shahat and R. Y. A. Hassan, *Biochem. Eng. J.*, 2025, **216**, 109660.
61 J. Gayathri, A. Roniboss, S. Sivalingam and K. S. Selvan, *RSC Adv.*, 2024, **14**, 16056–16068.
62 N. M. Nor, S. N. Nasrul, N. D. Zakaria and K. A. Razak, *ACS Omega*, 2023, **8**, 16587–16599.
63 N. M. Nor, S. Arivalakan, N. D. Zakaria, N. Nilamani, Z. Lockman and K. A. Razak, *ACS Omega*, 2022, **7**, 3823–3833.
64 S. Soman, P. V. Aswathy and R. Kala, *J. Polym. Res.*, 2021, **28**, 359.
65 J. Zou, D. Mao, Arramel, N. Li and J. Jiang, *Appl. Surf. Sci.*, 2020, **506**, 144672.
66 X. Zhu, B. Liu, H. Hou, Z. Huang, K. M. Zeinu, L. Huang, X. Yuan, D. Guo, J. Hu and J. Yang, *Electrochim. Acta*, 2017, **248**, 46–57.
67 F. Gao, N. Gao, A. Nishitani and H. Tanaka, *J. Electroanal. Chem.*, 2016, **775**, 212–218.
68 G. G. Matlou, D. Nkosi, K. Pillay and O. Arotiba, *Sens. Bio-Sens. Res.*, 2016, **10**, 27–33.